Available online at www.sciencedirect.com

ScienceDirect

International Journal of Multiphase Flow 34 (2008) 427–436

International Journal of Multiphase Flow

www.elsevier.com/locate/ijmulflow

Interfacial aeration and bubble count rate distributions in a supercritical flow past a backward-facing step

L. Toombes [a,1], H. Chanson [b,*]

[a] Connell Wagner, 433 Boundary Street, Spring Hill 4000, Australia

[b] Division of Civil Engineering, The University of Queensland, Brisbane QLD 4072, Australia

Received 11 October 2006; received in revised form 16 January 2008

Abstract

An example of high-velocity open channel flows is a supercritical flow past an abrupt drop. In such a geometry, the basic air–water flow properties were measured, including distributions of void fraction and bubble count rate, and local air and water chord size distributions, at and downstream of the backward-facing step. The bubble count rate distributions were compared with a conceptual model of streamwise distribution of air and water chords which yields a quasi-parabolic relationship between bubble count rate and void fraction. The proposed model was an attempt to explain the experimental relationship between bubble count rate and void fraction, rather a meticulous breakdown of the complex air–water structure.

Keywords: Air–water flows; Interfacial aeration; Bubble count rate; Surface waves; Water jet; Abrupt drop

1. Introduction

High-velocity open channel flows are extremely turbulent flows and interfacial aeration is commonly observed. A typical example is a supercritical open channel flow past an abrupt drop which consists of a water jet, followed by nappe impact and a downstream aerated flow (Fig. 1). In the flow regions where the void fraction C exceeds 0.3, the microscopic two-phase flow structure is complex, and it consists of a wide range of entities including air–water projections, foam, and complicated air–water imbrications (e.g., Thandavesvara, 1974; Volkart, 1980). Brocchini and Peregrine (2001) discussed the air–water interfacial zone in terms of intermittency. Some studies showed that maximum bubble count rates are typically observed for $0.4 < C < 0.6$ (Chanson, 1997; Toombes, 2002), although no physical explanation was proposed.

It is the aim of this work to provide some new information on the air–water flow properties (void fraction, bubble count rate, chord size distribution) in a high-velocity open channel flow past a backward-facing step (Fig. 1). The results are compared with a model of the streamwise distribution of air and water chords, and the role of surface waves is discussed.

2. Experimental setup

New experiments were performed in two open channels (Table 1). One channel was 0.25 m wide and 3.2 m long ending with a free overfall. The flume was equipped with a 0.143 m high step to investigate in details the millimetric and sub-millimetric air–water flow properties at and downstream of the drop (Fig. 1B). The second flume was 0.5 m wide and equipped with a stepped invert consisting of several 0.143 m high steps, although the study focus was on the first drop. Both channels had supercritical inflow conditions: $2 \leqslant Fr_0 \leqslant 10$ where Fr_0 is the approach flow Froude number. For all experiments, nappe ventilation by sidewall splitters was provided.

* Corresponding author. Tel.: +61 7 33653516; fax: +61 7 33654599.
E-mail address: h.chanson@uq.edu.au (H. Chanson).

[1] Formerly: Division of Civil Engineering, The University of Queensland, Brisbane QLD 4072, Australia.

0301-9322/$ - see front matter © 2008 Elsevier Ltd. All rights reserved.
doi:10.1016/j.ijmultiphaseflow.2008.01.005

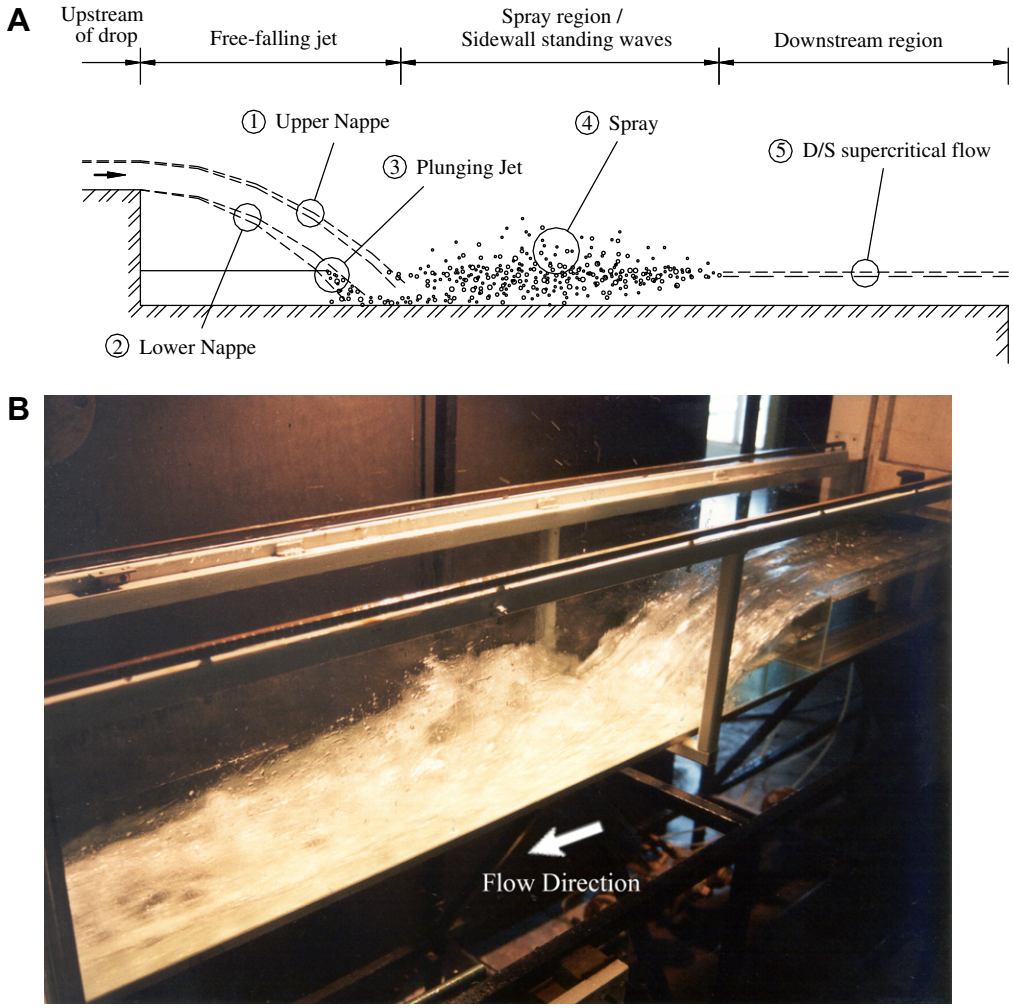

Fig. 1. Experimental configuration of supercritical flows past an abrupt drop: (A) definition sketch and basic air entrainment processes and (B) photograph of flow on Channel 2 – flow direction from top right to bottom right.

Table 1
Experimental flow conditions

Ref.	W (m)	h (m)	d_0 (m)	q_w (m^2/s)	d_c/h	Re	Comments
Channel 1	0.5	0.1433	0.030	0.080–0.150	0.6–0.92	3.2 to 6E + 5	Horizontal timber steps. Sidewall offset for nappe ventilation at 1st drop
Channel 2	0.25	0.1433	0.024–0.040	0.07–0.140	0.5–0.88	2.8 to 5.6E + 5	Single horizontal perspex step and glass flume. Sidewall offset (6.5 mm on each side) for nappe ventilation at drop

Notes: d_c: critical flow depth; d_0: approach flow depth; h: step height; Re: Reynolds number defined in terms of hydraulic diameter; and W: channel width.

The water flow rates were measured with a V-notch weir in the 0.25 m wide channel and with a Dall™ tube flowmeter, calibrated on site, for the 0.5 m wide flume. Clear-water flow depths and velocities were measured with a point gauge and a Prandtl–Pitot tube ($\emptyset = 3.3$ mm), respectively. The air–water flow properties were measured using either a single-tip conductivity probe ($\emptyset = 0.35$ mm) or a double-tip conductivity probe ($\emptyset = 0.025$ mm) developed at the University of Queensland. The probes were aligned in the flow direction and excited by an air-bubble detector (DSIR AS25240). The resistivity probe signals were scanned at 8 kHz for 180 s and 40 kHz for 40 s, respectively for the single-tip and double-tip resistivity probes. The translation of the probes in the direction normal to the channel invert was controlled by a fine adjustment travelling mechanism connected to a Mitutoyo™ digimatic scale unit. Further information and details were provided in Toombes (2002).

2.1. Upstream flow conditions

Water to the 0.25 m wide channel was controlled by a sluice gate located 0.62 m upstream of the backward-facing

step (Fig. 1). The approach flow conditions (d_0, V_0) were measured at vena contracta, where d_0 and V_0 are respectively the depth and velocity at the vena contracta downstream of the vertical sluice. The measured contraction ratio was between 0.63 and 0.68. At the step brink, the flow was partially-developed: i.e., $\delta/d_0 = 0.2$ to 0.35 where δ is the boundary layer thickness deduced from the velocity distributions measured with the Prandtl–Pitot tube.

The flow to the 0.5 m wide flume was fed through a smooth convergent nozzle (1.7 m long). The nozzle exit was 30 mm high and 0.5 m wide, and the measured contraction ratio was unity (i.e., $d_0 = 30$ mm). The abrupt drop was located 2.4 m downstream of the nozzle exit. Earlier experiments showed that the flow was quasi-two-dimensional and fully-developed at the first drop (Chanson, 1995b).

2.2. Quality control and data accuracy

The phase-detection probe is a sensitive device that is susceptible to a number of problems. In the present study, the quality control procedure was developed and applied thoroughly. Specifically the probe signals were checked systematically for long-term signal decays often induced by probe tip contamination, short-term signal fluctuations caused by debris and water impurities, electrical noise and non-representative samples.

The water discharge was measured with an accuracy of about 2%. The error on the vertical position of the probe was less than $\Delta z < 0.025$ mm. The system (probe and travelling mechanism) was mounted on a trolley system. The accuracy on the longitudinal position of the probe was estimated as $\Delta x < 0.5$ cm. The accuracy on the transverse position of the probe was estimated as $\Delta y < 0.5$ mm. The error on the void fraction measurements was estimated as: $\Delta C/C = 4\%$ for $0.05 < C < 0.95$, $\Delta C/C \sim 0.002/(1 - C)$ for $C > 0.95$, and $\Delta C/C \sim 0.005/C$ for $C < 0.05$. The air–water velocities were computed with a cross-correlation technique. The analysis of the velocity field and chord length distributions implied no slip between the air and water phases. The error on the mean air–water velocity measurements was estimated as: $\Delta V/V = 5\%$. for $0.05 < C < 0.95$, $\Delta V/V = 10\%$. for $0.01 < C < 0.05$ and $0.95 < C < 0.99$ (e.g., Chanson, 1995b; Cummings and Chanson, 1997). With the two-tip conductivity probe, the minimum detectable bubble chord length was about 150 μm in a 3 m/s flow based upon a data acquisition frequency of 20 kHz per channel.

3. Basic air–water flow measurements

For all investigated flow conditions, the upstream flow was supercritical ($Fr_0 > 1$). Downstream of each step brink, a free-jet took place with a ventilated air cavity below. Visually strong interfacial aeration was observed at the upper and lower nappes. The free-jet impacted on the lower channel invert and the impact region was characterised by strong splashing and spray generation (e.g., Fig. 1B). Downstream of nappe impact, the flow remained supercritical at all times up to the overfall at the downstream channel end. No hydraulic jump was apparent but shock waves were seen for all investigated flow conditions. A definition sketch and a photograph are presented in Fig. 1.

Typical void fraction distributions are presented in Fig. 2 in the free jet, spray region and downstream supercritical flow region. In the free-jet, free-surface aeration appeared to be predominant at the lower jet interface. This is seen in Fig. 2A with a steeper void fraction gradient $\partial C/\partial y$ at the lower jet interface. In the impact region, the void fraction distributions exhibited a flatter shape (Fig. 2B). Further downstream, the distribution of void fraction had an inverted S-shape commonly observed of supercritical open channel flows (Fig. 2C).

The bubble frequency F_a, or bubble count rate, is the number of air-structures per second detected by the leading tip of the probe. Typical bubble count rate distributions within the lower air–water interface of the jet are shown in Fig. 3 as function of dimensionless height $(z - Z_{50})/(Z_{90} - Z_{10})$ and void fraction C in Figs. 3A and B, respectively, where z is the vertical height measured from the

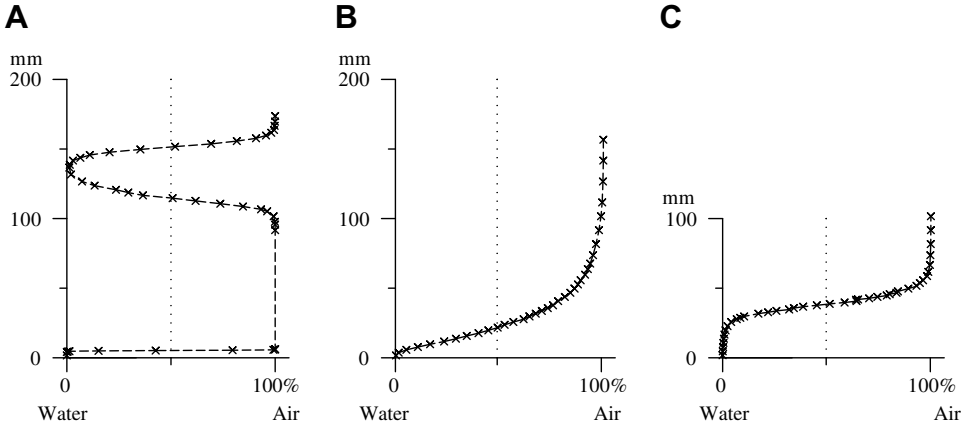

Fig. 2. Typical vertical distributions of void fraction – Channel 1, first drop, $d_c/h = 0.92$, $d_0/h = 0.21$, $Fr_0 = 9.2$, $Re = 6E + 5$, single-tip probe measurements, centreline data: (A) in the free-falling jet, (B) in the spray region and (C) in the downstream flow region.

Run	DT1	DT2	DT3	DT4	DT5
d_O/h	0.216	0.202	0.209	0.167	0.279
Fr_O	4.9	6.3	6.8	7.5	5.7
Re	3.4 E+5	3.9 E+5	4.4 E+5	3.5 E+5	5.7 E+5

(A) Vertical distributions

(B) Relationship between void fraction and bubble count rate - Comparison with Equations (1) and (3)

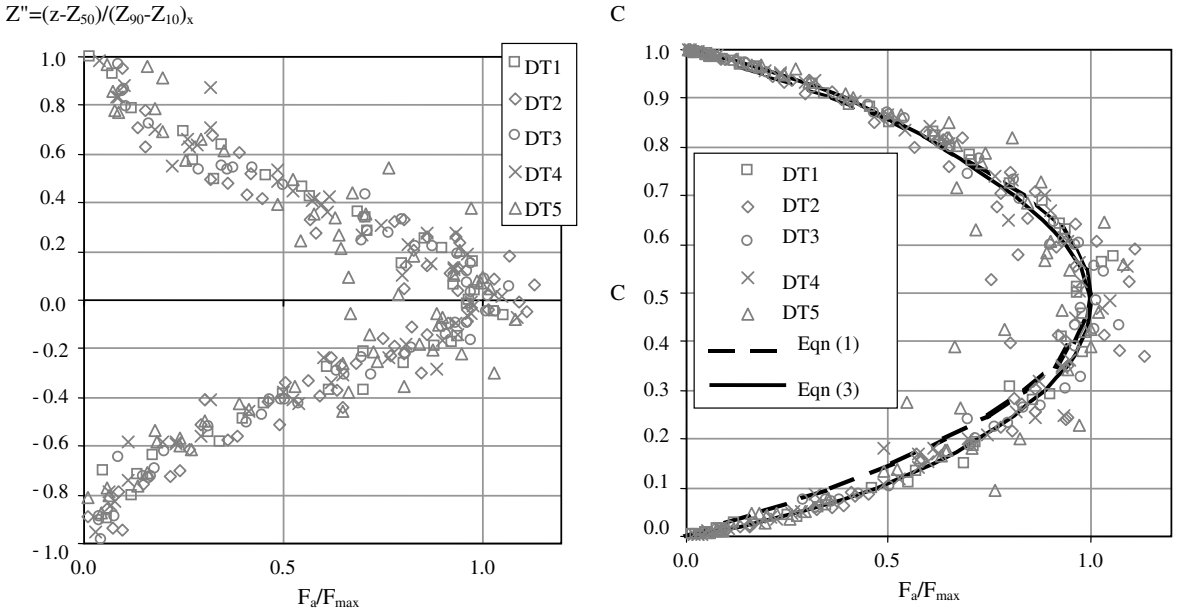

Fig. 3. Dimensionless distributions of bubble count rates at the lower jet interface (Channel 2, $h = 0.1433$ m, double-tip probe measurements): (A) vertical distributions and (B) relationship between void fraction and bubble count rate – comparison with Eqs. (1) and (3).

downstream channel invert, and Z_{10}, Z_{50} and Z_{90} are the characteristic heights where $C = 0.10$, 0.50 and 0.90, respectively.

All the present data suggested that the bubble-frequency distributions were correlated reasonably well by a parabolic law:

$$\frac{F_a}{F_{max}} = 4C(1 - C) \quad (1)$$

where C is the time-average void fraction and F_{max} is the cross-sectional maximum bubble count rate (Fig. 3B). Eq. (1) was observed in the free-jet, nappe impact region and downstream flow region. It is shown in Fig. 3B for the lower jet interface. Such a parabolic relationship was recorded in a number of other air–water flow situations, including supercritical open channel flows, two-dimensional free-falling jets and within the turbulent shear region of hydraulic jumps (e.g., Chanson, 1997; Chanson and Toombes, 2002). (These are not shown herein.) No physical explanation was proposed until now, while the experimental data tended to deviate from the parabolic relationship as shown in Fig. 3B for the present data.

3.1. Air/water chord size distributions

The chord size distributions present the variations in individual chord sizes of either air-bubbles or water-droplets passing a fixed point. They may be represented by a probability density function (PDF) or a cumulative distribution function (CDF). For all flow conditions at all locations, the experimental results showed a broad range of chord sizes from less than 0.5 mm to more than 25 mm. The PDFs were skewed with a preponderance of small chord sizes compared to the mean. The mode was typically between 0.5 and 2.5 mm. The PDFs exhibited a similar shape to a number of standard PDFs including the Gamma, Weibull and log-normal PDFs, but there was no clear-cut best fit.

Examples of probability density and cumulative distribution functions of both air and water chord sizes are shown in Fig. 4 for three different void fractions ($C \approx 0.25$, 0.50 and 0.75). All data were collected in the same section on the channel centreline at $x = 1.8$ m downstream of the backward-facing step where x is the horizontal distance measured from the backward-facing step, positive in the downstream direction. The data are presented in 0.5 mm chord size intervals and local air–water flow properties are given in the caption.

In Fig. 4, a 'modified' log-normal curve was fitted to the data. The 'modified' curve simply multiplied the standard log-normal PDF and CDF by a scaling factor less than unity. The artifice removed a certain percentage of chord-lengths from the sample distribution, but the 'modified' log-normal curve provided a good approximation of the

Figure	C	F_a (Hz)	$(ch_a)_{mean}$ (mm)	$(ch_a)_{mean}$ (mm)
(A) Top	0.24	249	3.1	9.8
(B) Middle	0.48	288	5.6	6.1
(C) Bottom	0.76	205	12.5	4.0

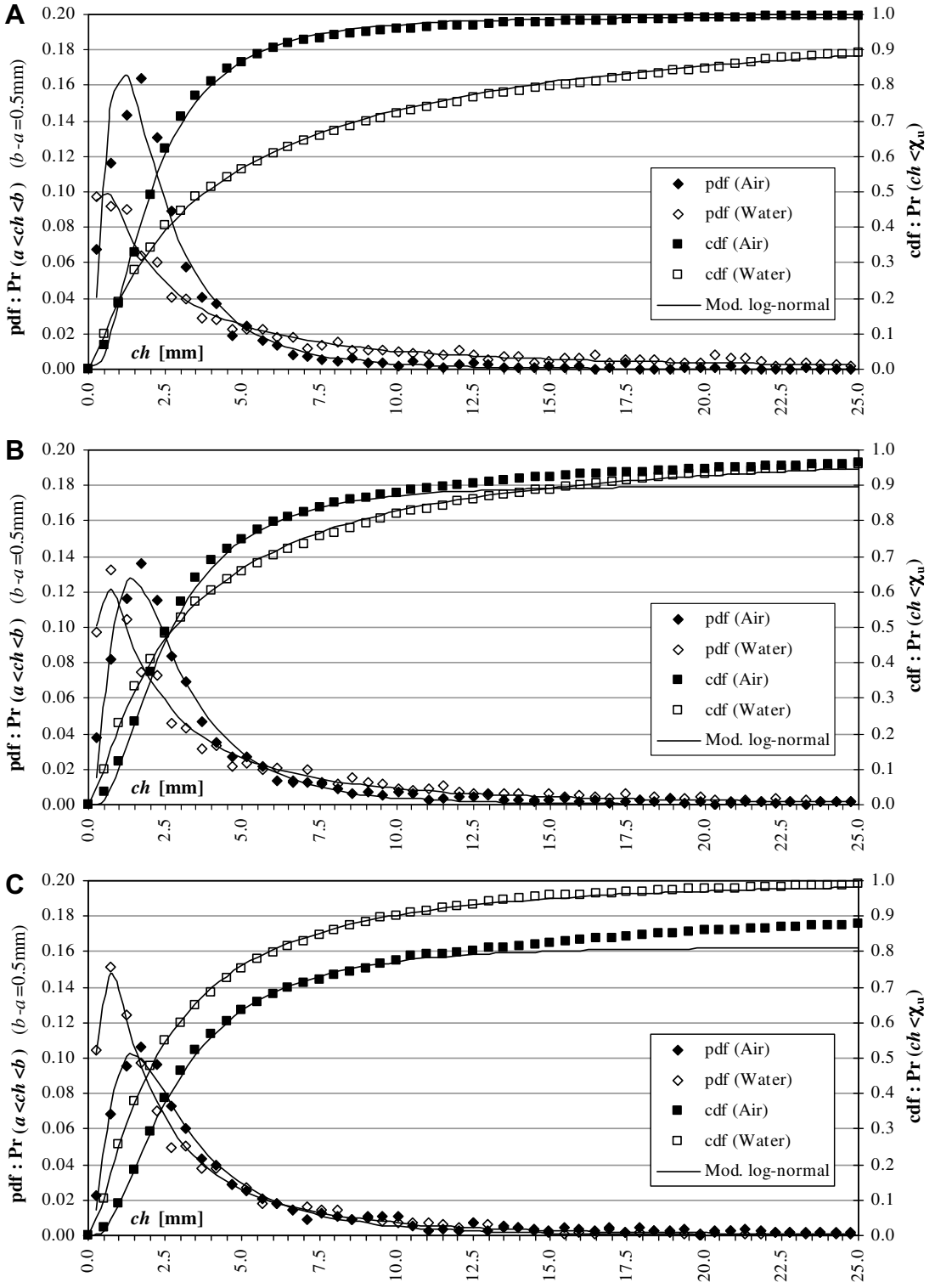

Fig. 4. Probability distribution functions and cumulative distribution functions of chord sizes: Channel 2, $Fr_0 = 6.8$, $Re = 4.4E + 5$, $d_0/h = 0.209$, double-tip probe, $x = 1.8$ m (downstream flow region).

smaller measured chord lengths in both PDFs and CDFs. An additional probability function, representative of the larger chord sizes, must be added to obtain the true distribution (e.g., Toombes, 2002).

In Fig. 4, note the noticeable difference between air-bubble and water-droplet distributions at $C \approx 0.50$. An exact explanation cannot be provided without direct knowledge of the nature of air–water structures. One possibility alluded to by visual observations is that the air-concentration profile at a fixed point on the step undergoes a periodic variation with time (see below).

4. Bubble count rate distributions – a theoretical model

The bubble count rate is a function of the average bubble chord-length, which in turn is a function of the shape and size of the bubbles, surface tension forces, and shear forces in the fluid. The prediction of the effect of air concentration on bubble frequency is a complex process. A simplified analogy is to picture the air–water mixture flow past a fixed point (e.g., probe sensor) as a series of discrete one-dimensional air and water elements (Fig. 5). The elements may have any size distribution, but the typical size of discrete air and water elements are given by the length scales λ_a and λ_w, respectively. The size of discrete water and air elements, λ_a and λ_w, is a function of the fragmentation of the flow: e.g., a highly fragmented flow (λ_a and λ_w small) will have a high bubble frequency.

The streamwise distribution of air and water chords may be 'constructed' by linking these discrete elements together in a 'random' order (Fig. 5). The probability of any discrete element to be air is the void fraction C assuming that each segment is either air or water. Conversely, the probability of any discrete element to be water is the liquid fraction $(1 - C)$. Each air-bubble is bounded by a transition from water to air and air to water. Assuming that $\lambda_a = \lambda_w$ and that the probability of an element being air or water is independent of the state of adjacent elements, the bubble count rate is derived from the probability of consecutive elements being air and water as:

$$F_a = \frac{V}{\lambda_a} C(1 - C) \tag{2}$$

where V is the air–water velocity (App. I). When V and λ_a are constant in the section, the maximum frequency occurs for $C = 0.5$ with $F_{max} = V/(4 \times \lambda_a)$ resulting in the parabolic relationship (Eq. (1)).

A better predictive model is derived by introducing two correction factors α and β that are functions of the local void fraction and flow conditions:

$$F_a = \frac{V}{\alpha\beta\lambda} C(1 - C) \tag{3}$$

where λ is a constant length scale factor. Basically λ is a length scale such that the probability of a discrete element of that size being air or water is independent of the surrounding segments. In Eq. (3), the correction factor α accounts for the average size of discrete air elements λ_a having a different value to the average size of water elements λ_w at any given point. α may be derived from a simple probability analysis (App. I) as:

$$\alpha = 1 + C \times \left(\frac{\lambda_w}{\lambda_a} - 1\right) \tag{4}$$

The correction factor β allows for variations of discrete element length scales λ_a and λ_w with the void fraction:

$$\beta = 1 - b(1 - 2C)^4 \tag{5}$$

where the coefficient b is a constant characteristic of the maximum variations of β with $(1 - b) \leqslant \beta \leqslant 1$. Although the correction factor α has some theoretical justification (App. I), Eq. (5) is an empirical correlation derived from the best fit of experimental data.

Eq. (3) is compared with experimental observations in Fig. 3B and 6. The values of λ_w/λ_a and b for the best data fit are summarised in Table 2 assuming the ratio λ_w/λ_a to be a constant independent of the void fraction C. The coefficient b was about 0.4 for most flow situations, but some variations of λ_w/λ_a were observed which might reflect differences in air–water flow structures between the free-jet, impact region and downstream supercritical flow (Table 2). In particular, the variations of λ_w/λ_a might be the result of a surface wave phenomenon in the downstream flow region (see below).

Gonzalez (2005) tested and applied the above model to his experimental data in skimming flow on a stepped chute with Reynolds numbers between 8E + 4 and 8.7E + 5 (Gonzalez, 2005, pp. 74–78). His results are also summarised in Table 2.

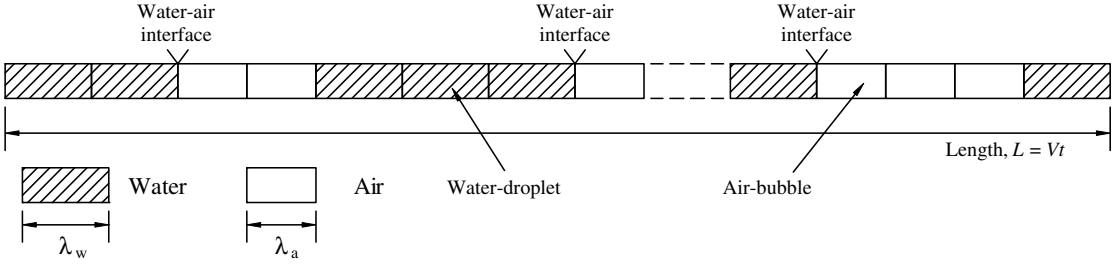

Fig. 5. Simplified model of streamwise distribution of an air–water mixture.

Run	DT1	DT2	DT3	DT4	DT5
d_O/h	0.216	0.202	0.209	0.167	0.279
Fr_O	4.9	6.3	6.8	7.5	5.7
Re	3.4 E+5	3.9 E+5	4.4 E+5	3.5 E+5	5.7 E+5

(A) Jet impact region (x = 1.0 m)

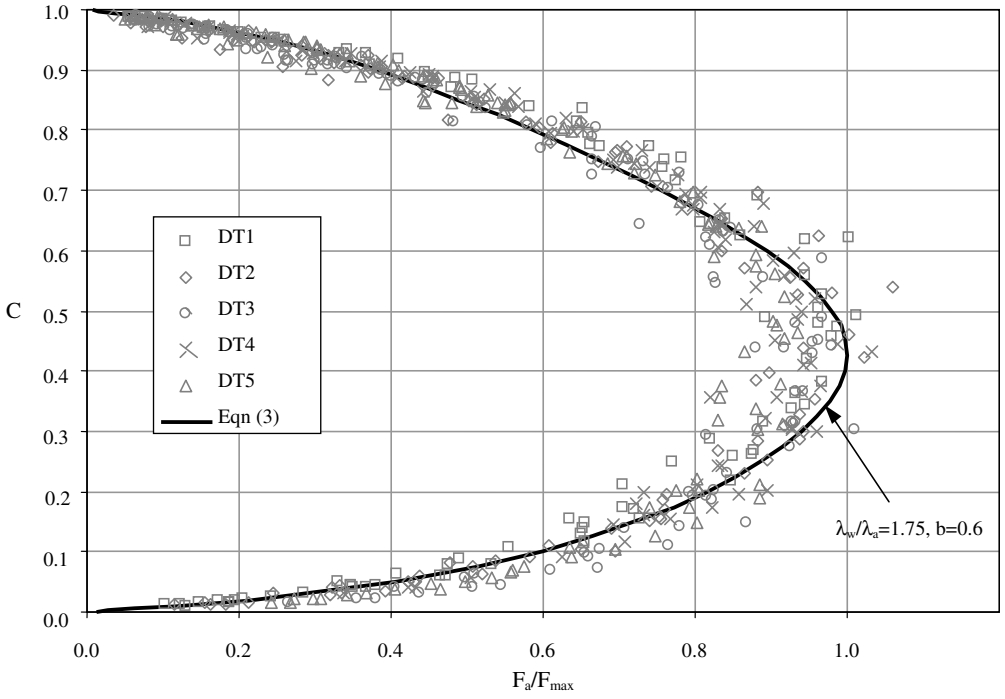

(B) Downstream flow region (x= 1.8)

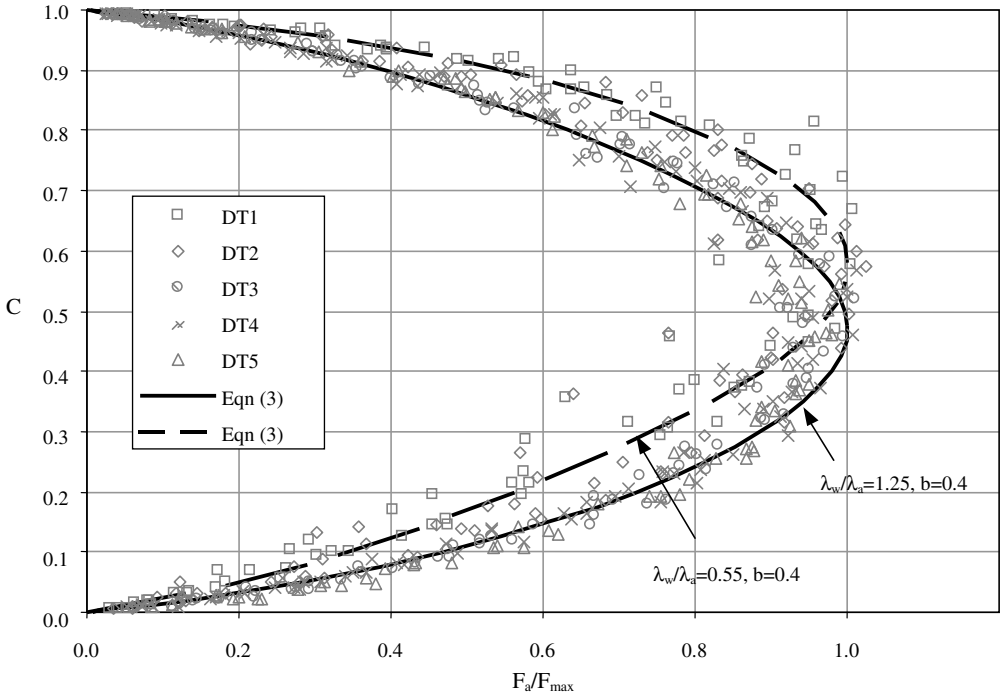

Fig. 6. Dimensionless distributions of bubble count rates – comparison between Eq. (3) and experimental data (Channel 2, $h = 0.1433$ m, double-tip probe measurements): (A) jet impact region ($x = 1.0$ m) and (B) downstream flow region ($x = 1.8$ m).

Table 2
Observed values of the coefficients λ_w/λ_a and b (Eqs. (3) and (4))

Flow region	λ_w/λ_a (Eq. (4))	b (Eq. (5))	Remarks
Present study (Channel 2)			$Re = 2.8$–$5.6E+5$
Free jet			
Lower nappe	1.25	0.4	$0 < x <$ jet length
Upper nappe	1.0	0.4	$0 < x <$ jet length
Spray and impact region	1.75	0.6	
Downstream flow region	0.55–1.25	0.4	Supercritical flow with cross-waves
Gonzalez (2005)			$Re = 8E+4$–$8.7E+5$
Transition flow on stepped chute	1.75	0.41–0.71	
Skimming flow on stepped chute	1.75	0.43–0.64	

Note: x: horizontal distance measured from the vertical step face.

4.1. Remarks

The length scaling of λ_a and λ_w is such that the probability of a discrete element of that size being air or water is independent of the surrounding segments. In a region of low void fraction ($C \to 0$), the length of air segment λ_a is equal to the average chord-length of single air-bubbles. Conversely, in a region of high air concentration ($C \to 1$), the length λ_w is equal to the average chord-length of single water-droplets.

Eq. (3) implies that the maximum bubble frequency F_{max} occurs for $C = C_{F_{max}}$ which may be approximated by:

$$C_{F_{max}} \approx \left(\sqrt{\frac{C(1-C)}{\alpha}}\right)_{F_{max}} \quad \text{for } \lambda_a \neq \lambda_a \tag{6}$$

The maximum bubble frequency is about:

$$F_{max} \approx \frac{V}{\lambda} C^2_{F_{max}} \tag{7}$$

Eqs. (6) and (7) were derived from Eq. (3) assuming $b = 0.4$ and $0.5 \leqslant \lambda_w/\lambda_a \leqslant 2$. The maximum error for Eqs. (5) and (6) is 0.5% and 0.05%, respectively. Finally Eq. (3) may be rewritten:

$$\frac{F_a}{F_{max}} = \frac{C(1-C)}{\alpha\beta C_{F_{max}}} \tag{8}$$

The modified parabolic relationship (Eq. (3) or (8)) is not intended to be a meticulous breakdown of a complex air–water structure, but rather is an attempt to model the relationship between bubble count rate and void fraction based upon simple theory and observed behaviour. However, its application was successful as demonstrated by Fig. 3B and 6. For completeness, further successful comparisons were performed in skimming flows above stepped chutes (Gonzalez, 2005).

5. Discussion

An intrusive phase-detection probe, such as the conductivity probe used in this study, detects the passage of air–water interfaces at a fixed point. It is nearly impossible to differentiate between true 'air-bubbles' (or 'water-droplets') and a structure that is not enclosed: e.g., a surface wave or a surface roughness. During the present study, a noticeable fluctuation, or wavy pattern, was visible at the free surface in the downstream flow region. A simple numerical model was developed to simulate the air–water flow past a fixed-location probe (Toombes, 2002). The simulation assumes a set of 'base' distributions of void fraction, bubble count rate and bubble chord sizes, then modifying these in response to a periodic fluctuation of the flow depth somehow similar to the wavy interface model of Brocchini and Peregrine (2001). The 'base' air–water flow properties were assumed to comply with commonly accepted models: i.e., Chanson's (1995a) analytical model of void fraction distributions, Eq. (1) for bubble count rate distributions, and log-normal PDF of chord sizes as observed in supercritical open channel flows by Chanson (1997). Several types of periodic fluctuations of flow depth were tested. The surface wave length and amplitude were represented by Weibull probability distributions. All conditions satisfied locally continuity between void fraction, count rate and chord size distributions. Fig. 7A shows two examples of investigated surface wave models while Fig. 7B presents typical air–water structures detected by a probe sensor at a fixed location in a wavy air–water flow.

The simulation results indicated that the presence of free-surface wave can modify significantly the shape of bubble count rate distributions. The latter might be simplistically represented by the ratio λ_w/λ_a. If $\lambda_a < \lambda_w$, the peak bubble count rate occurs for $C < 0.5$ and the result is a 'surface wave' profile similar to that sketched in Fig. 7A(a), for which the variations caused by the wave pattern increase with flow depth and time-average void fraction. Conversely, a wave profile or 'bubble surge' as sketched in Fig. 7A(b) corresponds to a ratio $\lambda_w/\lambda_a < 1$. Although there is no definitive evidence that low values of λ_w/λ_a observed at the downstream end of the channel (Table 2) are solely the result of free surface wave pattern, some effect is likely.

Numerical simulations were unable to model exactly the experimental observations of chord sizes distributions due to the simplistic nature of the surface wave model. However the numerical results tended to corroborate the theory that there exists a bubbly transition from water to air, with the shape of the air concentration modified by a semi-regular wave pattern. It is suggested that, in the bubbly flow only (eliminating the wave influence), the air and water chord distributions might be fitted by a standard log-normal distribution, and that the 'abnormal' percentage of large chord sizes (e.g., Fig. 4) might be the result of a wave pattern or variations of the water depth with time.

6. Summary and conclusion

The basic air–water flow properties (void fraction, bubble count rate, chord size distributions) were investigated in

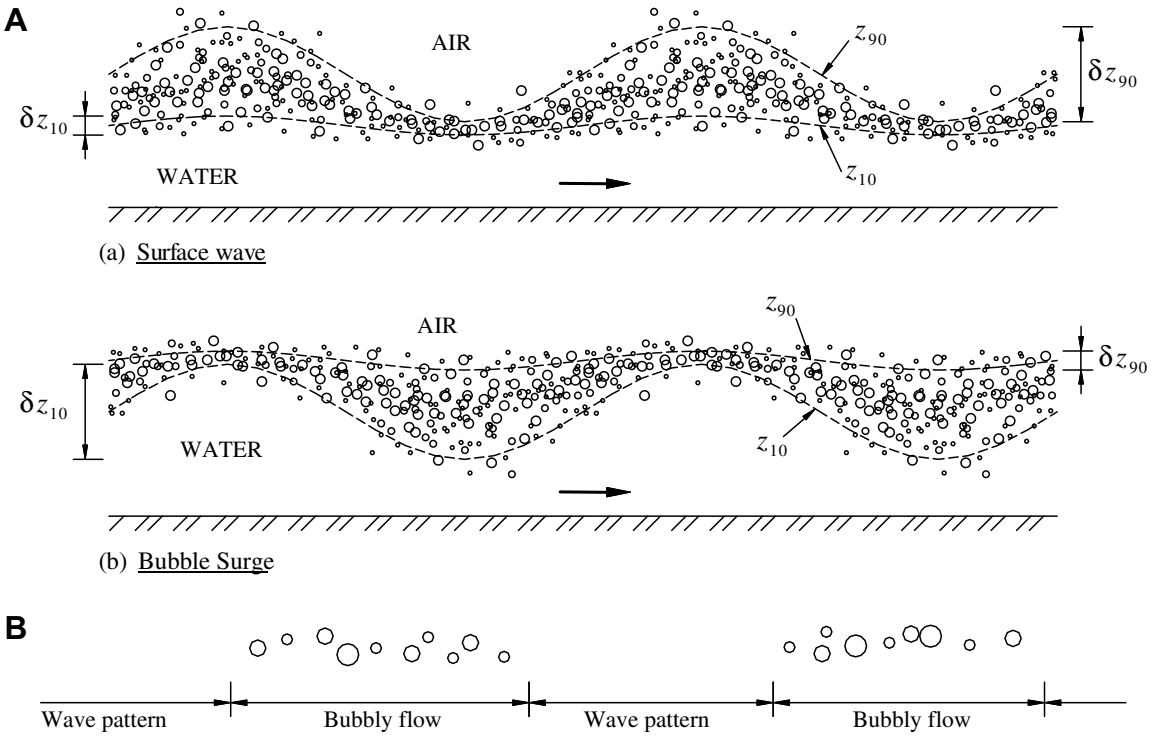

Fig. 7. Schematic of surface waves in supercritical open channel flows: (A) hypothetical sketches of surface waves in supercritical open channel flows and (B) air–water flow structure detected by a probe sensor fixed in space in a wave affected bubbly flow.

supercritical open channel flows past a backward-facing step. The experimental investigations were conducted with precise instrumentation in the free-jet, at nappe impact and in the downstream supercritical flow region. The cross-sectional distributions of bubble count rate showed a quasi-parabolic relationship with the void fraction, while local chord size PDFs exhibited a quasi-log-normal shape. The results were found to be nearly independent of the measurement locations and inflow conditions within the range of the investigations (Table 1).

The bubble count rate distributions were compared with a model of the streamwise distribution of air and water elements yielding a quasi-parabolic relationship between void fraction and bubble count rate. The proposed relationship (Eq. (3)) was not intended to be a meticulous breakdown of the complex air–water structure, but rather an attempt to model the experimental relationship between bubble count rate and void fraction based upon a simple theory. The role of surface waves is discussed, suggesting that some free-surface waves might modify the shape of bubble count rate distributions.

Acknowledgements

The writers thank Mr G. Illidge for his assistance and Professor C.J. Apelt his valuable advice. The first writer acknowledges the financial support of the Australian Research Council and University of Queensland.

Appendix A. Bubble count rate distributions: discrete element hypothesis

The relationship between bubble count rate and time-average void fraction at a section was observed to be approximately parabolic in a number of flow situations. An explanation for this relationship has not been previously explored.

Considering a hypothetical section of a bubbly flow passing a fixed point at constant velocity, V for a period of time, t. The sample length is $L = Vt$ (Fig. 5). If the signal is divided into N equal segments, the length of each segment λ is given by: $N = L/\lambda = Vt/\lambda$. If each discrete segment is either entirely air or entirely water, the probability that any given segment is air equals the void fraction C. Practically, C is the probability of a probe-tip being in air during the scanning time. It is equal to the true void fraction if there is no slip. Similarly, the probability that any given segment is water is equal to the liquid fraction $(1 - C)$.

The bubble count rate F_a is the number of water-to-air interfaces detected by the probe sensor per second. Taking a single arbitrary segment, the segment marks the beginning of an air-bubble if the segment is air and the previous segment was water. Assuming that the probability for a segment to be in air or water is independent of the state of the adjacent segments, the probability of a segment being associated with one water–air interface is equal to: $C(1 - C)$. The total number of water-to-air interfaces in

the sample will on average be equal to: $NC(1-C)$. Hence the bubble frequency F_a is equal to the number of water–air interfaces per second:

$$F_a = \frac{NC(1-C)}{t} = \frac{V}{\lambda} C(1-C) \quad \text{(A-1)}$$

Considering the same section of air–water flow (Fig. 5) except that the air and water elements have different discrete length scales denoted λ_a and λ_w, respectively. The length of the sample is:

$$L = N_a \lambda_a + N_w \lambda_w = Vt \quad \text{(A-2)}$$

where N_a and N_w are respectively the number of air and water elements in the sample. The time-average void fraction equals:

$$C = \frac{N_a \lambda_a}{N_a \lambda_a + N_w \lambda_w} \quad \text{(A-3)}$$

The probability that a given discrete segment is air is $N_a/(N_a + N_w)$. The average total number of water–air interfaces in the sample is equal to: $N_a N_w/(N_a + N_w)$. Combining with Eqs. (A-2) and (A-3), the bubble count rate equals:

$$F_a = \frac{V}{\alpha \lambda_a} C(1-C) \quad \text{(A-4)}$$

where α is defined as:

$$\alpha = 1 + C\left(\frac{\lambda_w}{\lambda_a} - 1\right) \quad \text{(A-5)}$$

In effect, the correction factor α skews the parabolic relationship in the direction of the smallest discrete element length: e.g., if $\lambda_a < \lambda_w$, the peak bubble count rate F_{max} occurs for $C < 0.5$.

References

Brocchini, M., Peregrine, D.H., 2001. The dynamics of strong turbulence at free surfaces. Part 2: free-surface boundary conditions. J. Fluid Mech. 449, 255–290.

Chanson, H., 1995a. Air bubble diffusion in supercritical open channel flow. In: Bilger R.W. (Ed.), Proceedings of the 12th Australasian Fluid Mechanical Conference on AFMC, Sydney, Australia, vol. 2, pp. 707–710.

Chanson, H., 1995b. Air bubble entrainment in free-surface turbulent flows. Experimental Investigations. Report CH46/95, Department of Civil Engineering, University of Queensland, Australia, 368 pp.

Chanson, H., 1997. Air bubble entrainment in open channels. Flow structure and bubble size distributions. Int. J. Multiphase Flow 23, 193–203.

Chanson, H., Toombes, L., 2002. Air–water flows down stepped chutes: turbulence and flow structure observations. Int. J. Multiphase Flow 27, 1737–1761.

Cummings, P.D., Chanson, H., 1997. Air entrainment in the developing flow region of plunging jets. Part 2: experimental. J. Fluid Eng. Trans. ASME 119, 603–608.

Gonzalez, C.A., 2005. An experimental study of free-surface aeration on embankment stepped chutes. Ph.D. thesis, Department of Civil Engineering, University of Queensland, Brisbane, Australia, 240 pp.

Thandavesvara, B.S., 1974. Self aerated flow characteristics in developing zones and in hydraulic jumps. Ph.D. thesis, Department of Civil Engineering, Indian Institute of Science, Bangalore, India.

Toombes, L., 2002. Experimental study of air–water flow properties on low-gradient stepped cascades. Ph.D. thesis, Department of Civil Engineering, University of Queensland, Australia.

Volkart, P., 1980. The mechanism of air bubble entrainment in self-aerated flow. Int. J. Multiphase Flow 6, 411–423.